Nano-twinning enhanced room temperature fatigue crack growth in single crystalline CoCrFeMnNi high entropy alloy

R. Sidharth [a], W. Abuzaid [b], H. Sehitoglu [a,*]

[a] *Department of Mechanical Science and Engineering, University of Illinois at Urbana-Champaign, 1206 W. Green St., Urbana, IL, 61801, USA*
[b] *Department of Mechanical Engineering, American University of Sharjah, PO Box, 26666, Sharjah, United Arab Emirates*

ABSTRACT

The equiatomic high entropy alloy CoCrFeMnNi is known for its unique strain hardening behavior which extends to cryogenic temperatures and gives remarkable monotonic toughness. Studies show that activation of twinning at such low temperatures is the key factor for the exceptional mechanical properties of this alloy. However, room temperature deformation has been assumed to be slip dominated. If deformation twinning develops during room temperature fatigue crack growth (FCG) it could impart beneficial properties and the current paper focuses on single crystals exhibiting twinning at increasing crack lengths. The results are demonstrated for <001> single crystals and compared to the <111> single crystals. The various activated slip/twin systems influencing FCG were identified using high resolution digital image correlation (DIC) and electron backscattered diffraction (EBSD). Threshold stress intensity value for crack initiation and the Paris slope were unambiguously established. K^{max} for <001> and <111> samples extracted from precise displacement measurements turn out to be as high as 230 MPa-m$^{0.5}$ and 195 MPa-m$^{0.5}$ respectively, which far exceeds most materials. Concurrently, high resolution EBSD revealed extensive nano-twinning at the crack tip for the <001> case. EBSD results also elucidate slip-twin interactions and dislocation induced lattice rotation inside twinned volumes. In conjunction, TEM images from the crack tip confirm the presence of deformation twins and additionally reveal twin-twin interactions. Moreover, the local crack tip R-ratio (K^{min}/K^{max}) turns out to be much higher (>0.6) than the global R-ratio ($\sigma^{min}/\sigma^{max}$) due to the accumulation of large crack tip strains (>20%). Synchronously, the crack tip displacement profiles from DIC point to the absence of crack closure. Thus, extensive strain hardening of the material ahead of the crack tip without the loss of ductility due to activation of twinning results in the remarkable intrinsic damage tolerance for CoCrFeMnNi high entropy alloys.

1. Introduction

Commercially pure metals rarely exhibit the desirable properties for extensive structural use. For thousands of years, by exploiting metallurgical processing techniques such as alloying and heat treatment, humans have manipulated metals to obtain desirable set of properties. The adopted methods have been primarily optimized for alloys comprising a single principle element with minor addition of other elements. Strength and ductility can be optimized under such conditions, however, the inverse relation between these two extremely important aspects continued to pose a significant challenge. The recent development of multi-principle element alloys has garnered immense interest in the scientific community due to their high strength, ductility and fracture toughness, all at the same time [1–3]. These alloys are typically comprised of 5 or more principle elements in near equiatomic proportions. Due to the high configurational entropy (>1.6R), as opposed to conventional alloys with low configurational entropy (<0.7R), such systems are often referred to as high entropy alloys (HEA) [1–3]. Owing to the high configurational entropy contribution to the Gibbs free energy, there are countless possible HEA compositions through the combination of various elements across the periodic table that can exist as a solid solution without forming brittle intermetallic phases. To name a few, $Al_{13}CoCrFeNi$ [4], $CuCoNiCrAl_2Fe$ [5], TaNbHfZrTi [6], CoCrFeMnNi [7], out of which CoCrFeMnNi, which primarily exhibits a single phase (face-centered cubic FCC), has gained much attention due to its high strength and ductility exceeding 500 MPa and 50% even at cryogenic temperatures.

The mechanical properties of FCC CoCrFeMnNi have been

* Corresponding author.
 E-mail address: huseyin@illinois.edu (H. Sehitoglu).

extensively studied in both polycrystalline and single crystalline form at various deformation temperatures. The high strength levels have been attributed to massive solid solution strengthening and severe lattice distortion effect [1] leading to high lattice friction (Peierls stress) for dislocation motion. At cryogenic temperatures, ductility enhancement has been associated with deformation twinning which allows higher hardening levels and delays the onset of necking [8–11]. Thus, at room temperature and above, slip dominates, and deformation twinning can only be observed at very high deformation levels close to fracture [12, 13]. The scarcity of twinning at RT is partially a result of a considerable temperature dependence of yield stress which is not typical for FCC alloys [8]. This fact along with observations of a temperature independent critical twinning stress allow for twinning to occur only at a high critical stress achieved by extreme cooling or following significant hardening. A larger contribution from deformation twinning at RT deformation would be advantageous allowing for higher strength and ductility levels. In studies conducted in high manganese TWIP steels, Hamada et al. [14] reported superior fatigue limit compared to austenitic steels. Niendorf et al. [15] investigated the fatigue crack growth (FCG) behavior of TWIP steels and found that the FCG kinetics is slower for TWIP steels compared to other high strength steels. However, in their investigation, twinning could be realized only in monotonic loading and not during FCG. Absence of twinning during FCG, they say, preserves the ductility of the material ahead of the crack tip by significantly reducing the kinematic hardening rate and therefore promotes slower crack growth rate. However, in the current HEA being investigated, activation of twinning only at larger strains synergistically enhances ductility and hardening rate [16]. Thus, when dislocation slip mediated ductility is exhausted, activation of twinning could prove to be beneficial for a superior RT FCG characteristic.

While there have been some studies on monotonic strength and fracture toughness of CoCrFeMnNi HEA, there has been only one study on fatigue crack growth by Thurston et al. [10,17] in polycrystalline CoCrFeMnNi. This study was devoted towards exploring the effect of temperature and load ratio on threshold stress intensity range and the Paris law exponent for polycrystalline CoCrFeMnNi. To expedite the commercial availability of this promising material, a systematic study of the fatigue crack growth behavior from the viewpoint of orientation dependence of the threshold regime is necessary. Direct observations of crack tip deformation and its role in the crack growth process is required to unequivocally understand the interplay between the exceptional strain hardening behavior and the fatigue crack propagation in this material. For example, Neumann [18] and Smith et al. [19] both concluded in their study that plastic slip ahead of the fatigue crack is responsible for crack advance. Orowan [20], in 1949, proposed that ductile crack formation is almost always preceded by void nucleation and coalescence along the intersecting slip planes. Thus, fatigue crack propagation is expected to be affected by slip irreversibility ahead of the crack which is influenced by intersecting slip planes producing kinks and jogs which in turn increases the dislocation line tension, reduces dislocation mobility and gives rise to hardening. The extent of this hardening and the ability of the material to sustain more plastic deformation without leading to unstable fracture determines the fracture toughness of the material. Gludovatz et al. [9] pointed out that the monotonic fracture toughness, exceeding 200 MPa-m$^{0.5}$, exhibited by CoCrFeMnNi at cryogenic temperatures is due to plastic deformation mediated by twinning near the crack tip and it is absent at room temperatures. Thurston et al. [10], in their fatigue crack growth studies of polycrystalline CoCrFeMnNi, also observed that the benefits of twinning could be realized only at cryogenic temperatures. However, in this study, deformation twinning was observed during room temperature FCG in single crystals. Congruently, the room temperature maximum crack tip stress intensity exceeding 230 MPa-m$^{0.5}$ was recorded for these single crystals. Additionally, in the stage I regime, observations by Forsyth [21] in FCC aluminum points to inclined crack growth along the activated slip planes. Thus, both mode I and mode II stress intensities

need to be considered for accurate prediction of fatigue crack growth rates and threshold stress intensity values, which has been addressed in this study as well.

Another major factor affecting fatigue crack growth is crack closure induced by (i) surface roughness affected by the crack path, (ii) crack surface asperities due to oxidation and (iii) residual plasticity in the crack wake [22]. Plasticity induced crack closure was first introduced by Elber [23] in 1970. Before that, it was thought that crack closure only occurred during compressive loading. Elber proposed that the fatigue crack remains essentially closed even during the initial stages of the loading in the tensile half of the cycle. He stipulated that the plastically deformed material in the crack wake is constrained by the surrounding undeformed matrix which induces compressive tractions on the crack flanks. Thus, the crack remains closed until the crack opening load is reached and the portion of the fatigue cycle below the crack opening load does not contribute towards the crack tip driving force. After that many researches began computing effective stress intensity range for fatigue crack propagation as K^{max}-K^{open} as opposed to K^{max}-K^{min}. Elber measured crack closure using displacement gauges [24]. This method evolved into using back-face strain gages to detect the change of slope in the load vs displacement curves [25] indicating crack opening. With the recent advancement of non-contact optical techniques like digital image correlation to measure strains and near crack tip displacements, direct in situ observation of crack closure can be made [26]. Moreover, with the analytical description relating the crack tip stress intensities to near crack tip displacement fields given by Sih et al. [27], the stress intensity change per fatigue cycle can be extracted from the full field displacement measurements obtained via DIC which inherently accounts for crack closure. This technique has been used in many studies before to successfully calculate the stress intensity factors for both single crystalline and polycrystalline materials [28–31].

To this end, in this study, we explore the room temperature fatigue crack growth mechanism in single crystalline CoCrFeMnNi with the tensile axis oriented parallel to <111> and <001> directions. The use of single crystals allows us to study the orientation dependence of the threshold stress intensity factor for fatigue crack initiation which needs clear insight. Both Mode I and Mode II contributions to the fatigue threshold and fatigue crack growth parameters are considered as the crack growth is expected to occur along crystallographic slip planes. Crack tip shielding influenced by crack closure and crack tip deformation modes are explored through in-situ crack tip displacement and strain measurements via DIC. Ex-situ high resolution DIC measurements are performed to reveal the slip systems active in the vicinity of the notch prior to crack initiation and the crack growth direction is linked to the activated slip systems. The extent of crack closure in both the orientations is tracked by noting the change in the local R-ratio (K^{min}/K^{max}) at the crack tip with crack advance. In addition, postmortem high-resolution electron back scattered diffraction (EBSD) analysis with a step size of 20 nm was carried out at the crack tip to reveal the various deformation modes at play and the lattice rotation induced due to crack tip dislocations by visualizing the local misorientation. Thus, this study attempts to provide a comprehensive understanding of fatigue crack growth behavior in FCC high entropy alloy CoCrFeMnNi by linking the pertinent mechanisms active across various length scales.

2. Materials and methods

Single crystalline ingot of equiatomic CoCrFeMnNi was grown using Bridgeman technique in helium atmosphere. The ingot was homogenized at 1473 K for 24 h followed by quenching in water. Dog bone tension samples with 3×1.5 mm^2 cross-section were electric discharge machined (EDM) from the ingots with tensile axis parallel to <111> and <001> crystallographic directions. The crystal orientations were confirmed through electron backscatter diffraction (EBSD). A circular notch of 0.18 mm width, 90 μm radius and 0.5 mm depth (i.e. initial a/W of 0.17) was EDM cut into the sample's gauge section. Prior to loading

all the samples were solution treated at 1373 K for 1 h to dissolve undesirable sigma phase [32], if any, and quenched in oil. Subsequently the samples were sequentially polished using SiC abrasive papers from 300 Grit down to 0.05 μm suspended alumina. Then a speckle pattern was applied on the sample surface by air blasting 1200 grit SiC powder.

Fatigue crack growth experiments were carried out using an Instron servo hydraulic load frame at 1 Hz frequency. The <001> oriented samples were cycled in stress control between 130 MPa and 6.5 MPa and the <111> samples were cycled between 160 MPa and 8 MPa with a global R-ratio of 0.05. In-situ images were captured during the test using an IMI-Tech 1200FT optical camera at the rate of 15 frames per second, 1200 × 1600 pixels resolution and 5× magnification corresponding to 0.87 μm/pixel. These images were used to obtain full-field strain and displacement values via a commercially available DIC software (VIC-2D, Correlated Solutions). The test was periodically slowed down to 0.2 Hz every 3000 cycles to obtain sufficient images for accurate regression analysis of the crack tip displacement fields. In addition to in-situ measurements, high resolution ex-situ images were captured before and after deformation using an optical microscope at 20× magnification (0.2 μm/pixel resolution). 5 × 8 grid of images spanning an area of 1 × 1.6 mm^2 were captured in the vicinity of the notch and stitched together. The detailed procedure for in-situ and ex-situ DIC pertinent to fatigue crack growth studies have been elucidated in previous works [33,34]. Postmortem EBSD was carried out at the crack tip in JOEL 7000F cold FE SEM after attaining an acceptable sample surface quality by polishing as mentioned previously and finished with vibro-polishing in 0.02 μm colloidal silica for 4 h.

3. Experimental results

3.1. Notch tip strain field

In general, ductile and defect free metals exhibit plastic strain localization prior to the initiation of fatigue cracks. For the notched specimen geometry, the stress concentration results in localized plastic strain accumulation in the vicinity of the notch with cyclic loading due to slip irreversibility. For the single crystal specimens considered in this work (the <001> and <111> orientations), fatigue cracks were initiated in the notch area following cyclic loading. Due to orientation difference, which will affect stiffness and activated slip systems, each sample was cycled at a different stress level to eventually induce fatigue crack initiation. However, to further elucidate the role of plastic strain localization in the crack initiation process, the local response at the notch tip was monitored during the crack initiation stage (i.e., cyclic loading prior to crack initiation). Fig. 1 shows the accumulation of notch tip plastic strains following cyclic loading. The strain evolution in the vicinity of the notch over continued cycling follows the same trend for both orientations and eventually leads to initiation of a microcrack at the notch tip when the accumulated strain reached ≈2% in the DIC AOI after 13,000 cycles of fatigue loading in both the loading orientations investigated in this study. However, it should be noted that the high-resolution ex-situ DIC (obtained using the optical microscope) revealed a major difference between the two crystal orientations. It is evident from the strain contour plots (shown as insets in Fig. 1) that the strain distribution ahead of the notch tip is clearly different for both orientations. The difference in the number and orientation of localized strains bands highlight the different slip activity in terms of activated systems and number of activated systems.

3.2. Fatigue crack growth results

Fatigue crack growth experiments were conducted on three single crystals with loading orientations parallel to the <111> crystallographic direction and two single crystals with load orientations parallel to the <001> crystallographic direction. The full field vertical and horizontal crack tip displacements were obtained through DIC. These displacement
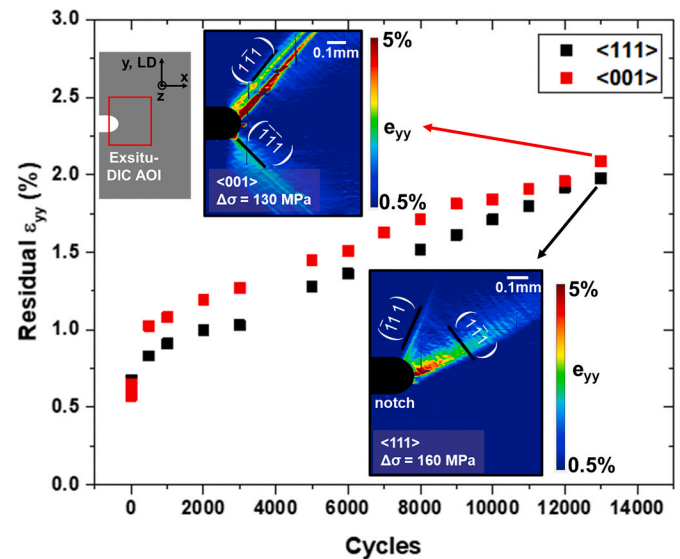

Fig. 1. Strain history at the notch top revealing the various slip systems active in both the loading orientations prior to crack initiation.

contours were regression fitted to the analytical expression for the displacement fields [27] to obtain the anisotropic stress intensity factors. The compliance constants used for the regression fitting were obtained from Ref. [35] and given in the appendix. Detailed procedure used for performing the regression analysis is explained in these studies [28–30,34] and briefly shown in the appendix for completeness. Both Mode I and Mode II stress intensity factors were combined [36] to obtain the total stress intensity range by employing equation (1) given below.

$$\Delta K_{total} = \sqrt{(\Delta K_I)^2 + \alpha(\Delta K_{II})^2} \tag{1}$$

Where α is the ratio between Mode II and Mode I energy release rates, J_2/J_1, which is given as follows [27],

$$J_1 = \frac{-\pi K_I}{2} a_{22} \text{Im}\left[\frac{K_I(\mu_1 + \mu_2) + K_{II}}{\mu_1 \mu_2}\right] \tag{2}$$

$$J_2 = \frac{\pi K_{II}}{2} a_{11} \text{Im}[K_{II}(\mu_1 + \mu_2) + K_I \mu_1 \mu_2] \tag{3}$$

Here a_{ij} are the compliance constants in the crack coordinate frame, μ_1 and μ_2 are the roots of the characteristic equation,

$$a_{11}\mu^4 - 2a_{16}\mu^3 + (2a_{12} + a_{66})\mu^2 - 2a_{26}\mu + a_{22} = 0 \tag{4}$$

The ratio of the energy release rates, α, was in the range of 0.1 – 0.2 for <111> and 0 for <001> orientation as the crack was tilted in the former and horizontal in the latter. The calculated total stress intensity range along with the crack growth rate were fit to the Paris equation given below to obtain the stable crack growth parameters.

$$\frac{da}{dN} = C(\Delta K_{total})^m \tag{5}$$

Fig. 2a below shows the crack growth rate vs the stress intensity range for <001> and <111> orientations. The Paris exponent for <001> orientation is lower than that of <111> with a value of 2.51 and 3.21 respectively. To investigate this further, crack tip strain fields were quantified and presented in the next section.

The displacement contours for regression fitting were obtained by performing DIC between the optical image captured at the start of the fatigue cycle and the image captured at the peak load of the same cycle. The maximum crack tip stress intensity is also shown in Fig. 2a using blue markers (includes both <001> and <111> orientations). This was
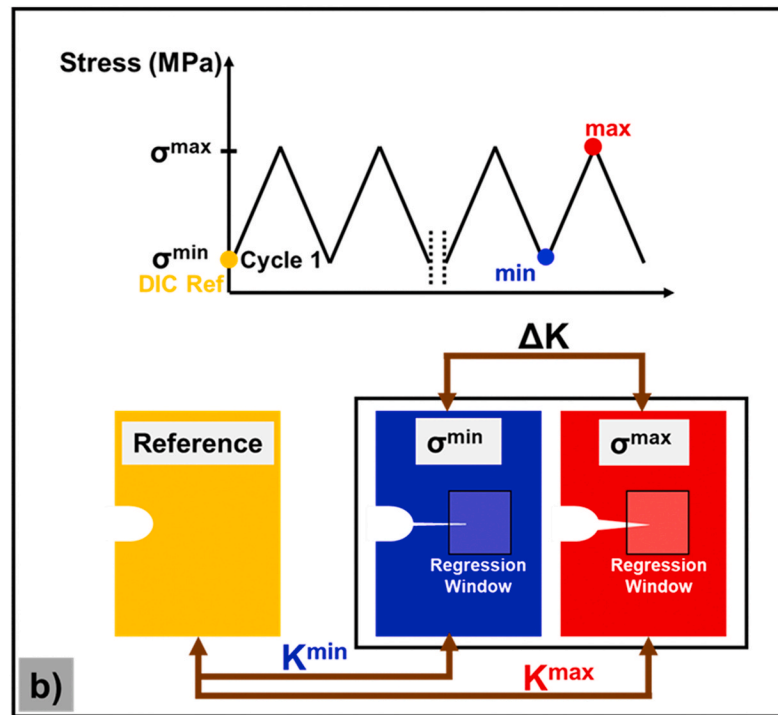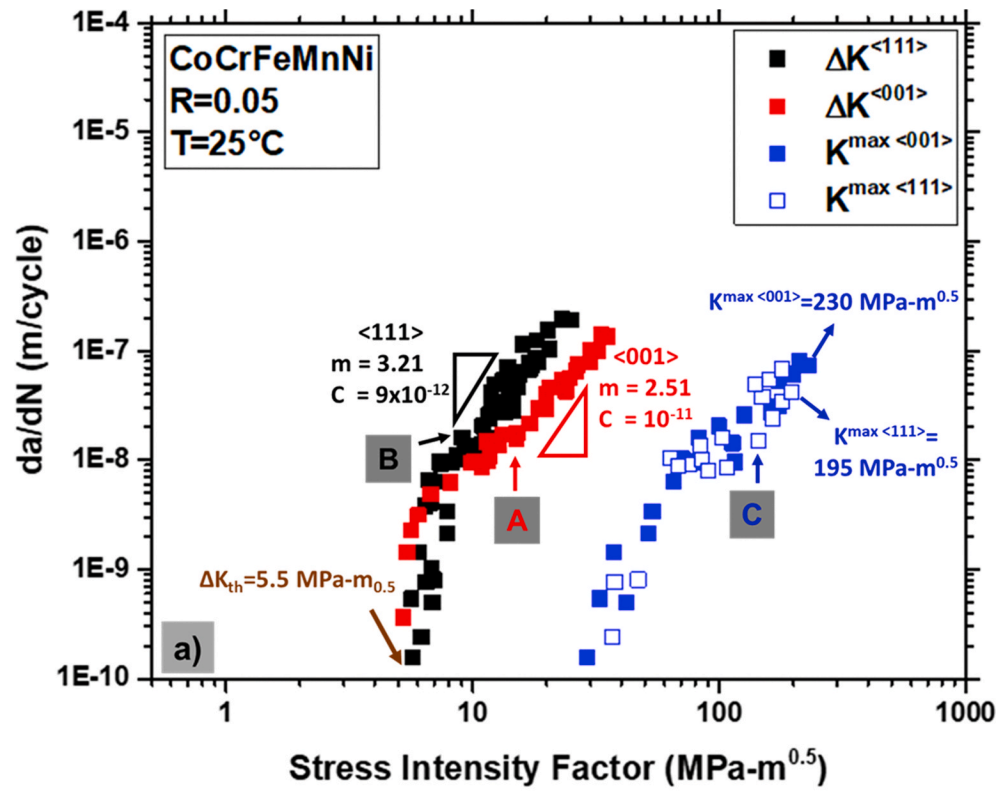
Fig. 2. a) Crack growth rate vs stress intensity factors obtained via regression for <001> and <111> orientations. The corresponding regression fits for the points marked as A, B and C are shown in Fig. 3 b) Schematic to illustrate the procedure for obtaining ΔK, K^{min} and K^{max} values.
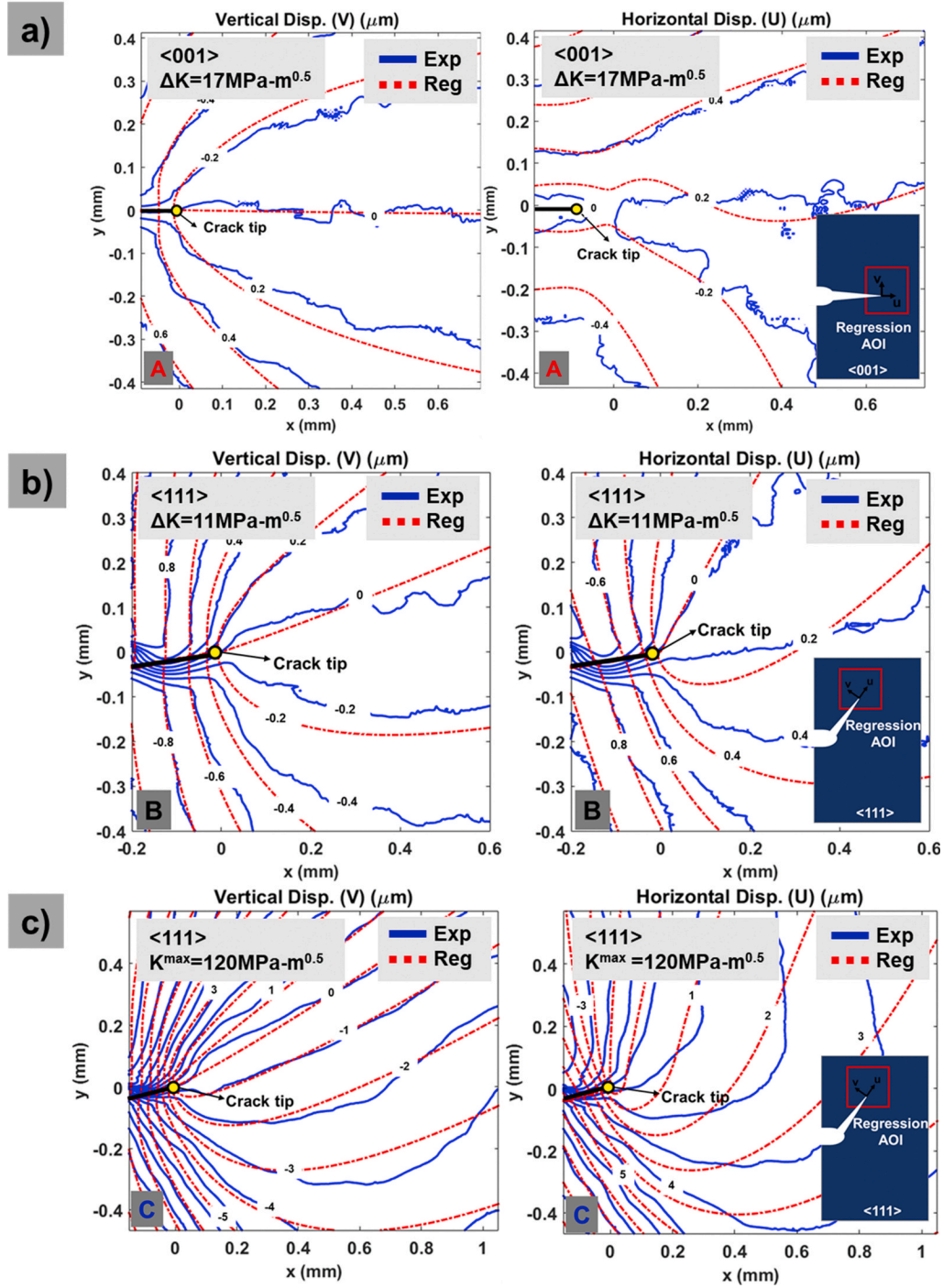
Fig. 3. Experimental displacement contours and the corresponding regression fits for a) $\Delta K^{<111>} = 11$ MPa-m$^{0.5}$ (point A, Fig. 2), b) $\Delta K^{<001>} = 17$ MPa-m$^{0.5}$ (point B, Fig. 2), and c) $K^{max} = 120$ MPa-m$^{0.5}$ (point C, Fig. 2). Note that the magnitude of the accumulated displacement contours to calculate K^{max} are 5 times the magnitude of displacement contours used for calculating ΔK.
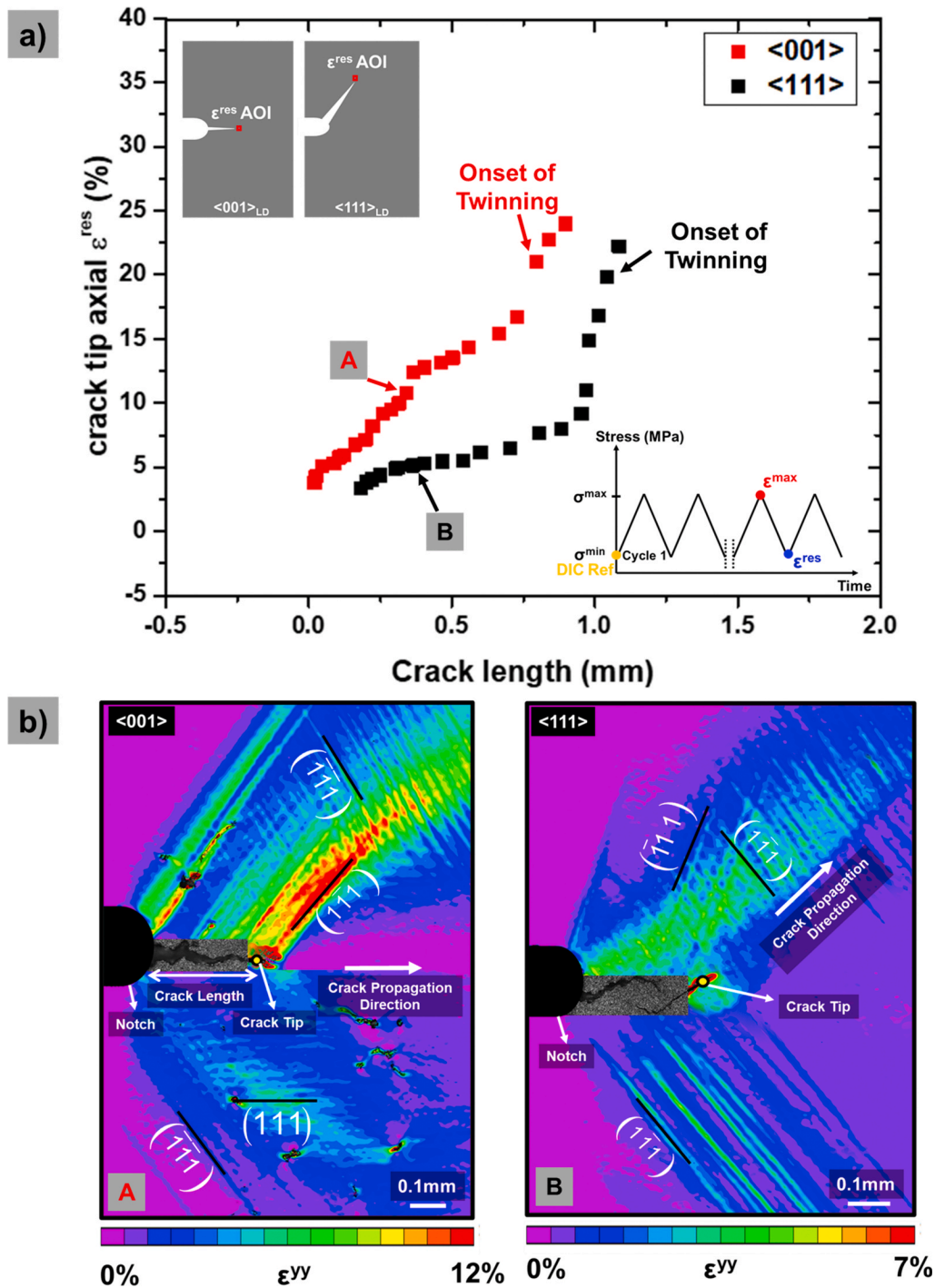
Fig. 4. a) Crack tip residual strain field plotted against crack length. b) The corresponding ex-situ DIC contours of the crack tip region in <001> and <111> loading directions depicting the different slip systems active around the crack tip. Note that the crack tip is illustrated with a yellow dot.
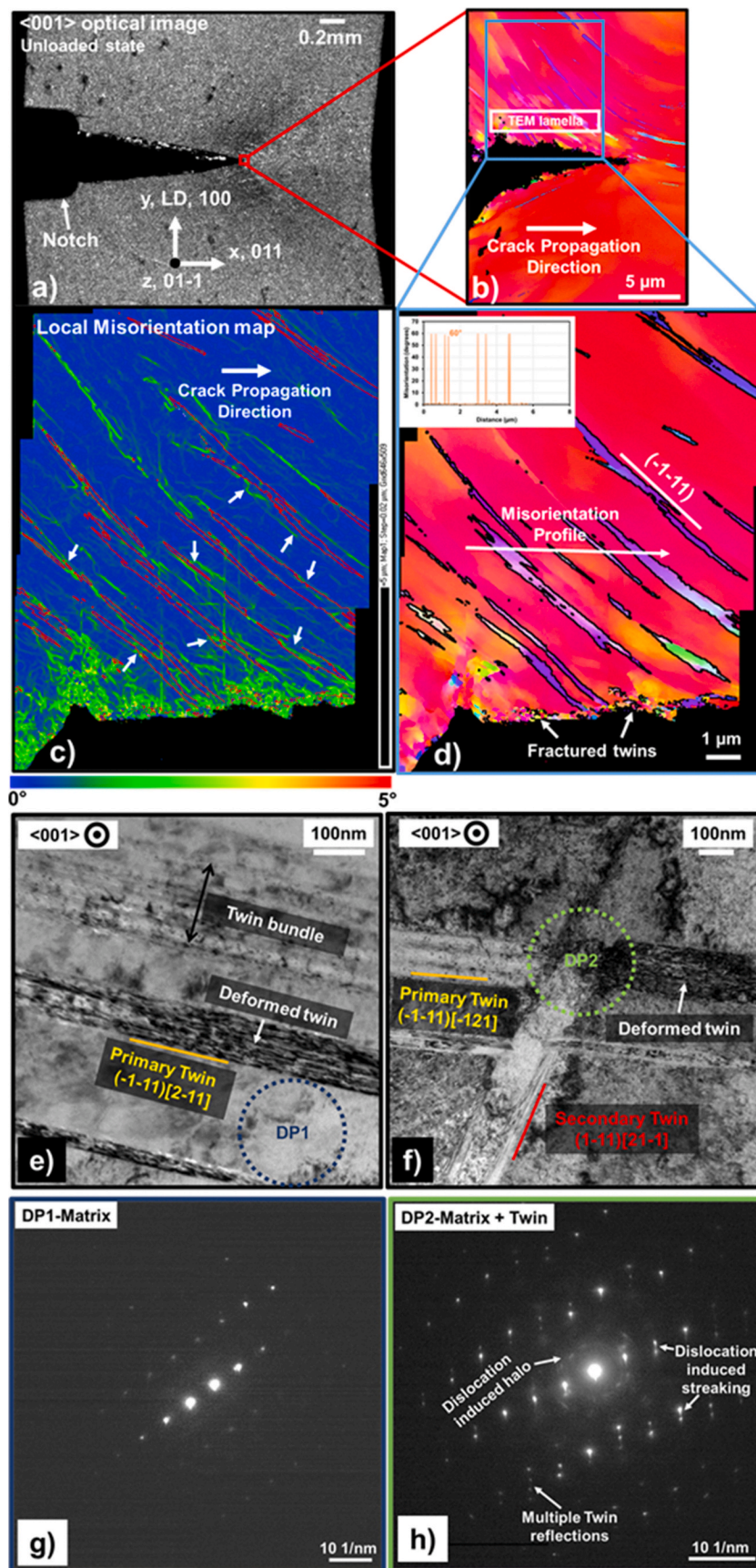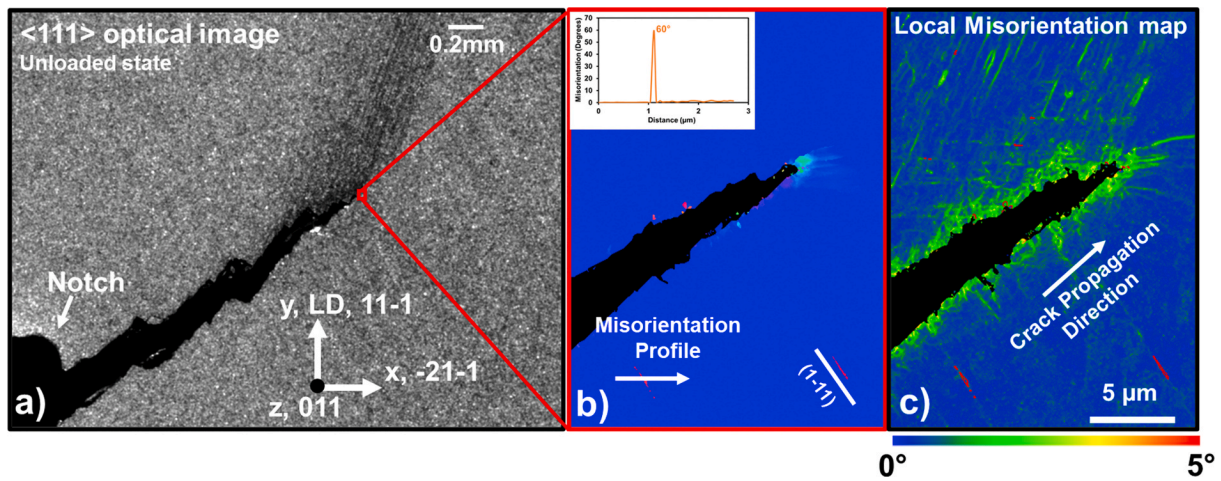
Fig. 5. a) Optical image of <001> sample in the unloaded state indicating the location of EBSD and the sample coordinate system. Note that the crack mouth opening displacement is ~160 μm. b) Corresponding EBSD map taken at low magnification (5000x). c) Local misorientation map corresponding to (d) revealing the extent of deformation near the crack. Note the localization of deformation i.e. local misorientation near the twin boundaries (white arrows) and close to the crack tip. d) 20 EBSD maps taken at 30 k magnification, 20 nm step size stitched together. Note the IPF coloring of the individual deformation twins in (d) and the equivalent local misorientation in (c) revealing dislocation induced misorientation within the twins and close to the twin boundaries. TEM images of the lamella taken from the location shown in (b) are presented in images e) and f). The corresponding SADP are shown in g) and h). Note the dislocation induced halo and streaking in the diffraction spots stemming from the twinned region. This is consistent with the local misorientation maps. Additionally, twin-twin interactions are visible in (f).

Fig. 6. a) Optical image of <111> sample in the unloaded state indicating the location of EBSD and the sample coordinate system. Note that the crack mouth opening displacement is ~115 μm. b) Crack tip EBSD revealing few sparsely spaced deformation twins and some fractured twins on the crack surface. c) Corresponding local misorientation map indicating high degree of deformation around the crack tip.
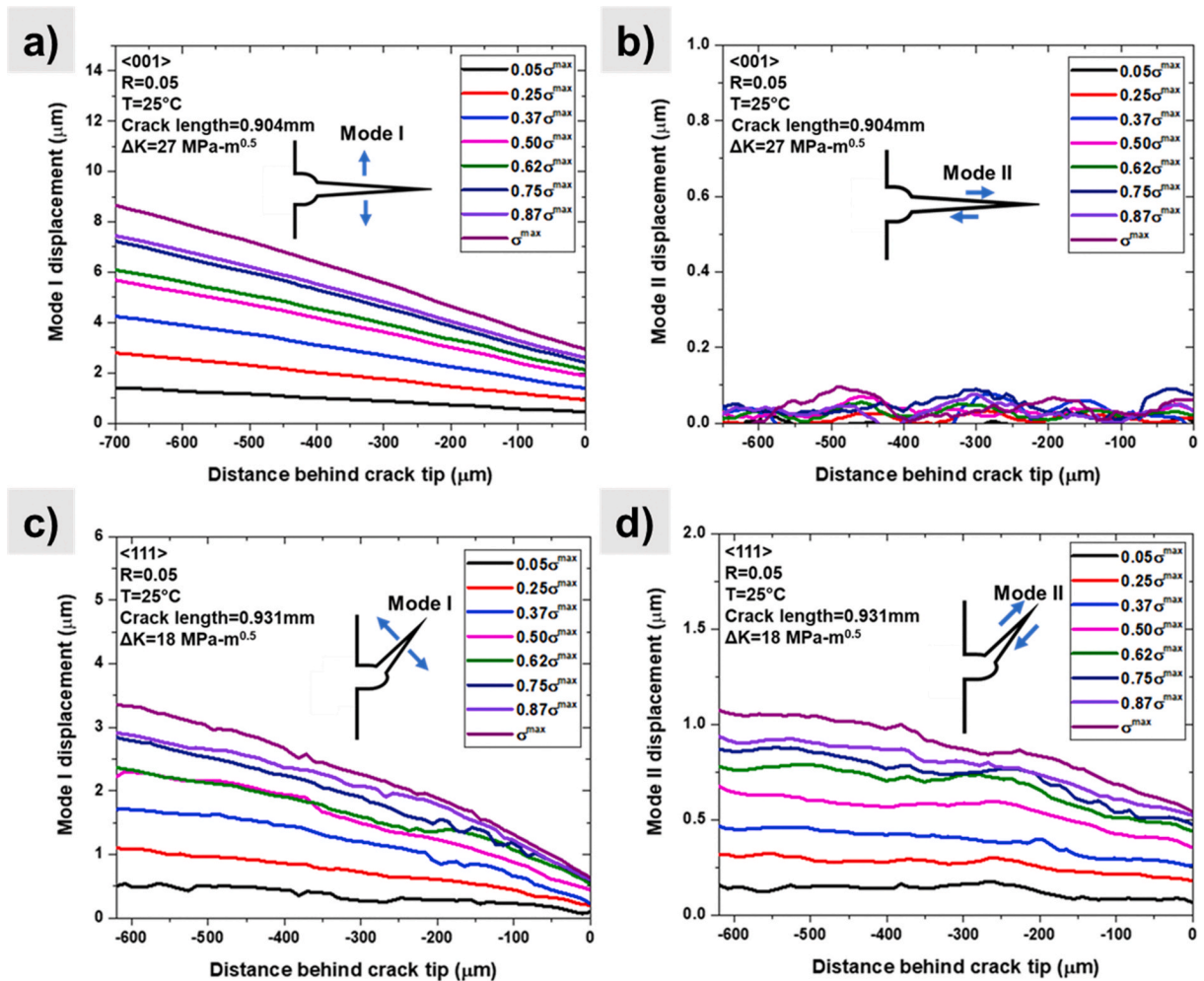

Fig. 7. a) Mode I and b) Mode II crack opening displacement profiles for <001> loading orientation at a crack length of 0.904 mm and $\Delta K = 27$ MPa-m$^{0.5}$. c) Mode I and d) Mode II crack opening displacement profiles for <111> loading orientation at a crack length of 0.931 mm and $\Delta K = 18$ MPa-m$^{0.5}$.

calculated by regression fitting the accumulated crack tip displacements obtained by performing DIC between the reference image captured before crack nucleation and the image captured at peak load of the fatigue cycle. The procedure for obtaining ΔK and K^{max} is schematically shown in Fig. 2b. The experimental displacement contours and the corresponding regression fits are shown in Fig. 3. A good agreement between the experimental and theoretical fits is evident and consistent throughout the entire analysis.
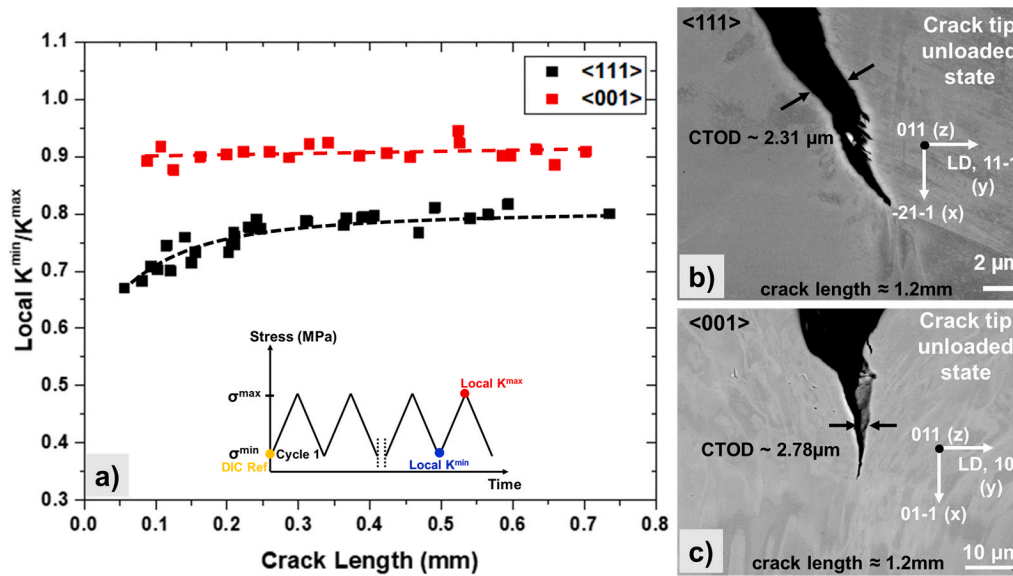
Fig. 8. a) Evolution of crack tip R-ratio with crack length for <001> and <111> loading orientations. SEM image of the crack tip in b) <111> and c) <001> samples respectively revealing the open crack tip in the unloaded state. The CTOD for <001> is around 2.78 μm and for <111> is around 2.31 μm at 10 μm behind the crack tip.

3.3. Crack tip plasticity

Crack tip strain field is of considerable importance to gain insight into the driving force for fatigue crack propagation in ductile solids. Due to the singularity in crack tip stress field formulations, it is difficult to accurately predict the crack tip strain field via analytical methods. Thus, a direct measurement of the strain fields is required and is only possible via full-field measurement techniques such as digital image correlation (DIC). Axial strain contours around the crack at various crack lengths during crack growth of <001> and <111> samples were obtained by correlating the optical image captured prior to crack initiation with the images captured at maximum load of each fatigue cycle. These results are portrayed in Fig. 4 below. The strains were obtained in a relatively small area of interest (AOI) ahead of the crack tip (marked as ε^{res} AOI in Fig. 4). It should be pointed out that the location of the crack tip AOI changes following crack advance. Therefore, the reported strains in Fig. 4 are always in un-cracked regions ahead of the advancing crack.

The full-field strain contour plots were also utilized to shed insight into the local slip system activity in the crack tip region. The strain contour plots (insets in Fig. 4) clearly show the localized strain bands associated with slip system activation. Three different slip systems (obtained via trace analysis) in the <001> orientation, at all crack lengths, were observed. On the other hand, only two slip systems are active for the <111> orientation. Intersection of multiple slip systems increases the strain irreversibility at the crack tip. This is evident in Fig. 4 for the <001> case. For example, at a crack length of 0.5 mm, the maximum strain at the vicinity of the crack tip is ≈ 5% for <111> and ≈13% for <001>. As the crack length reaches around 0.8 mm (a/W of 0.43), which corresponds to a crack tip strain value of ≈20%, complex stress field and high levels of local hardening results in the nucleation of mechanical twinning in the <001> case. This onset of twin nucleation was confirmed using EBSD as discussed below. Although twinning was observed in the <001> case, at a comparable crack length, no evidence of twinning was found in the <111> sample. It should be pointed out that the local plastic strain magnitudes differed significantly with much lower plastic strain accumulation in the <111> sample. Once the local strains amplified to about 20% following additional crack growth (around 1.2 mm and a/W of 0.57), signs of twin nucleation were observed for the <111> sample.

To confirm the presence of deformation twins, postmortem EBSD analysis was carried out at the crack tip for both the samples. EBSD was performed using a sub-micron step size to capture the nano-twins around the crack tip. Scan were collected at a crack length of 1.2 mm for <001> and <111> samples and shown in Figs. 5 and 6 below. Compared to <111>, <001> orientation had extensive nano-twinning at the crack tip. Crack tip EBSD for the <111> case is rendered in Fig. 6. Sparsely spaced twins are perceptible in <111> orientation (Fig. 6b, colored in red). Point to point misorientation profile (inset Fig. 6b) confirmed the presence deformation twinning. As the area fraction of deformation twins was significantly lower in <111> orientation, onset of nano-twinning was assumed to occur at the crack length of ≈1.2 mm (a/W of 0.57). The corresponding crack tip strain level was ≈20% as pointed out in Fig. 4 and the corresponding stress intensity range ($\Delta K^{<111>}$) at the onset of nano-twinning was 22.31 MPa-m$^{0.5}$.

The point to point misorientation profile taken across the EBSD map in the <001> case (see inset in Fig. 5d) reflects a misorientation angle of 60° confirming the presence of twins. Subsequently, 20 high resolution EBSD maps were captured at 30 K magnification and 20 nm step size on the upper portion of the crack to clearly resolve the nano-twins in the <001> case. There are some fractured twins decorated across the crack flanks in the <001> case indicating the activation of twinning ahead of the crack tip at an earlier crack length(<1.2mm). Assuming that the onset of twinning occurs at a crack tip strain of ≈20%, similar to <111> orientation, crack length of ≈0.8 mm (a/W of 0.43) was determined as the onset of twinning as indicated in Fig. 4. The corresponding stress intensity range ($\Delta K^{<001>}$) at the onset of nano-twinning was 26.83 MPa-m$^{0.5}$ which is comparable to that of <111>. TEM images taken from the crack tip of <001> additionally reveal twin-twin interactions on top of the slip-twin interactions.. Moreover, some of the twins have undergone further deformation as evident from the local misorientation maps in conjunction with the TEM images. The activated twin planes were identified via trace analysis. Average twin lamella width was measured to be ≈ 350 nm in <001> and ≈100 nm in <111>.

3.4. Crack tip R-ratio and crack opening displacements

Historically, the extent of fatigue crack closure was calculated by inferring the crack opening loads from load versus displacement curves
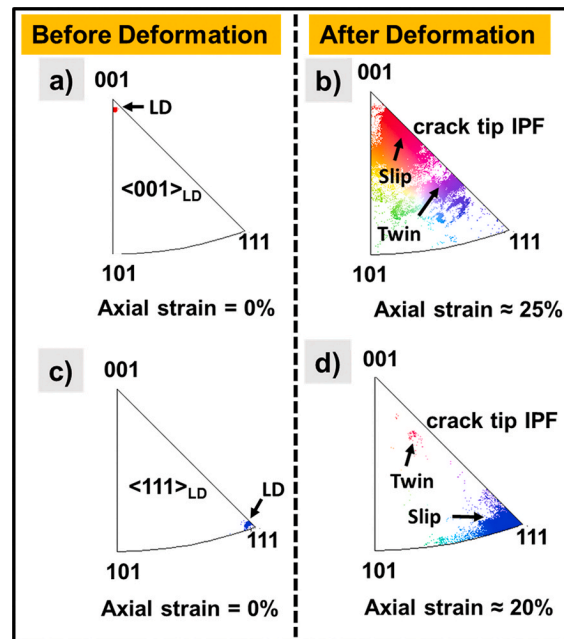
Fig. 9. IPF maps indicating deformation induced rotation of the lattice. a) Grip section IPF of <001> (no deformation), b) crack tip IPF of <001> (~25% axial strain), c) grip section IPF of <111> (no deformation), d) crack tip IPF of <111> (~20% axial strain). Note the spread in the IPF color of the twins in (b) which hints dislocation activity inside the crack tip nano-twins of <001>. LD indicates loading direction.

[23,24]. In this study, the local displacement measurements obtained through DIC were used to visualize crack closure. It has been found that, for both the orientations, crack tip remains open even at the minimum load of the fatigue cycle i.e. crack closure is absent in tension-tension fatigue of single crystalline CoCrFeMnNi. Mode I and Mode II crack opening displacements were extracted by the virtual extensometer technique illustrated in Ref. [29,37] and presented in Fig. 7 for crack lengths of 0.931 mm in the <111> case and 0.904 mm in the <001> case. The corresponding $\Delta K^{<111>}$ is ≈ 18 MPa-m$^{0.5}$ and $\Delta K^{<001>}$ is ≈ 27 MPa-m$^{0.5}$. For the <001> case, Mode II displacement was negligible as the crack growth was purely Mode I. On the other hand, in the <111> sample, both Mode I and Mode II displacements were substantial as the crack grew at an angle.

Previous studies have pointed out that the crack closure levels affect the effective R-ratio at the crack tip even if the applied global R-ratio is maintained constant [38]. To further demonstrate the repercussions of an open crack, the local crack tip R-ratio was tracked by noting the ratio of K^{min} and K^{max}. In this study, the K^{min} and K^{max} both reflect the local stress intensities at the crack tip as they were obtained through regression analysis of the accumulated displacement fields at the crack tip (see Fig. 2b). The change in local R-ratio with crack length shown in Fig. 8 below points to a prevalence of a non-zero crack tip stress intensity at the minimum load. Correspondingly, Fig. 8b and c show that the crack tip remains open even in the unloaded state. Additionally, as observed in a previous FEM study of crack growth in ductile materials [39], plasticity induced crack tip blunting during fatigue crack growth in this HEA could explain the open crack tip at minimum load and the consequent high K^{min} values. The possible origins of this is further contemplated in discussion section 4.3. It should be noted that crack tip blunting due to extensive local plastic deformation could render precise determination of crack tip stress intensities (K^{min} and K^{max}) difficult. However, we would like to point out that the regression fitting is dominated by the large displacements behind the crack tip which are predominantly elastic.

4. Discussion

4.1. Crack nucleation and early crack advance

Strain accumulation in the form of dislocation mediated slip acts as a precursor to crack initiation. Fatigue crack initiates when the total strain energy accumulation exceeds the surface energy for nucleating a crack [40,41]. As shown in this work, the CoCrFeMnNi Cantor alloy, which is well known for its exceptional ductility, accommodates high levels of plastic strain prior to the nucleation of fatigue cracks. For the two orientations, <111> and <001>, considered in this study fatigue cracks nucleated once the local axial strain reached $\approx 5\%$. In both cases, the localization and buildup of plastic strains were slip dominated with no evidence of deformation twinning. However, the number of activated slip planes differed which consequently affected the crack trajectory. In the <111> case, crack nucleation and propagation occurred at an angle of 40° along the intersection of $(\bar{1}11)$ and $(1\bar{1}1)$ slip planes (see Figs. 4b and 6a). In the <001> case two symmetric slip planes, $(1\bar{1}1)$ and $(\bar{1}\bar{1}1)$, were active and the crack nucleated and propagated nearly perpendicular to the loading direction along the intersection of the slip planes (see Figs. 4b and 5a).

The applied global stress range for <111> was 160 MPa and 130 MPa for <001> for crack initiation experiments. The higher stress range for <111> intuits an earlier crack nucleation compared to <001>. However, the crack nucleation occurred at approximately the same axial strain of 5% after going through $\approx 13,000$ fatigue cycles in both the orientations. This suggests that the strain accumulation in the form of dislocation pile-up at intersecting slip planes and the resulting resolved shear stress within the activated slip systems govern crack nucleation in this HEA. Consequently, the intrinsic threshold stress intensity range for fatigue crack initiation is similar (≈ 5.5 MPa-m$^{0.5}$) for both the orientations. The rather moderate intrinsic threshold stress intensity value obtained can be attributed to the absence of significant barriers to dislocation motion such as grain boundaries and particularly, coherent
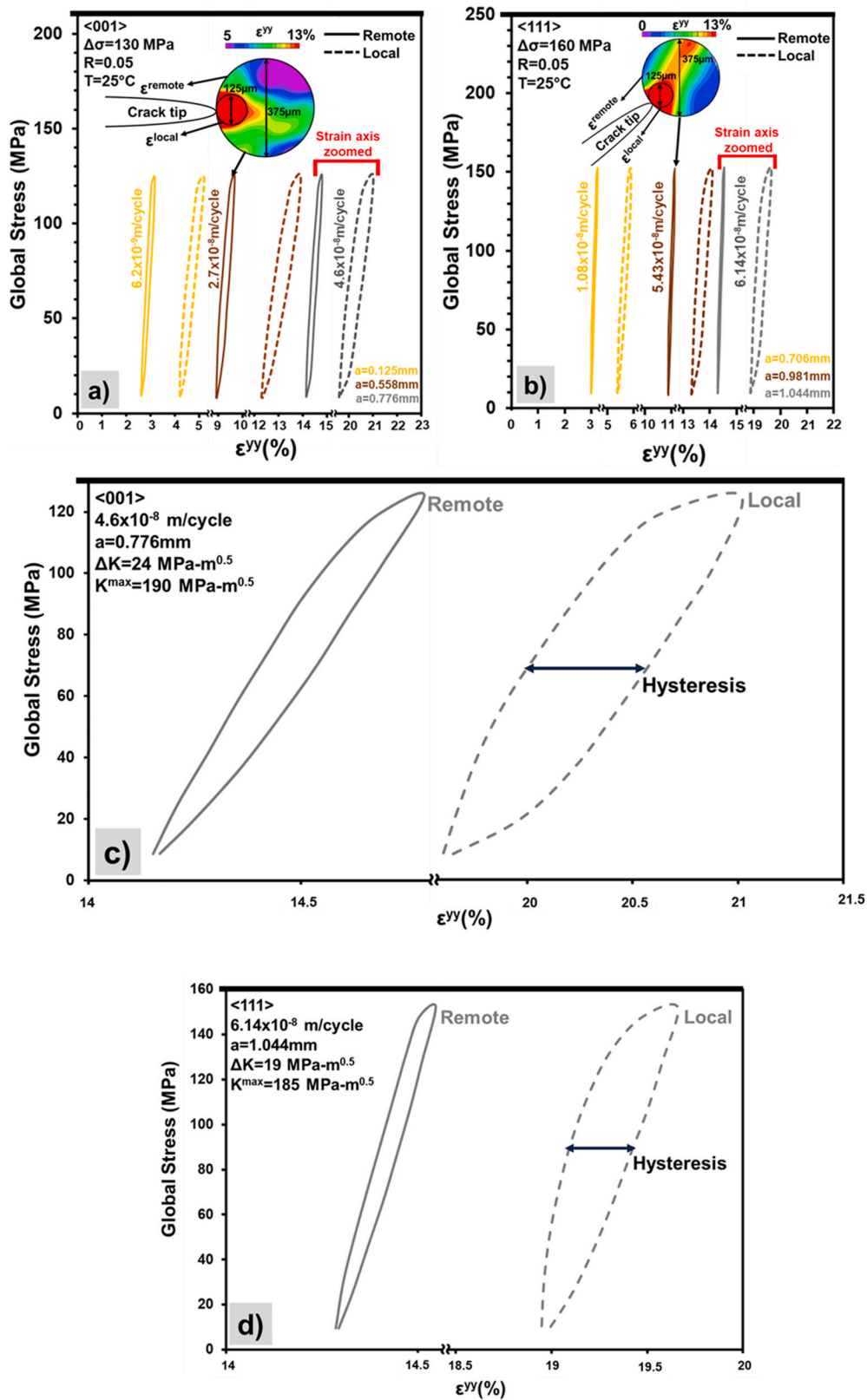
Fig. 10. Crack tip stress strain curves for a) <001> and b) <111> orientations at different crack lengths. The crack growth rate and the corresponding crack lengths are shown in Fig. 10a and b. Strain axis was zoomed for c) <001> and for d) <111> to clearly elucidate the differences in the hysteresis of the stress strain curves marked by the red bracket in Fig. 10a and b. Note that the stress vs local strain curves exhibit a smaller slope compared to the stress vs remote strain curves as the local curves are influenced by the crack opening. Note the exceedingly high local strains that CoCrFeMnNi can sustain near the crack tip.
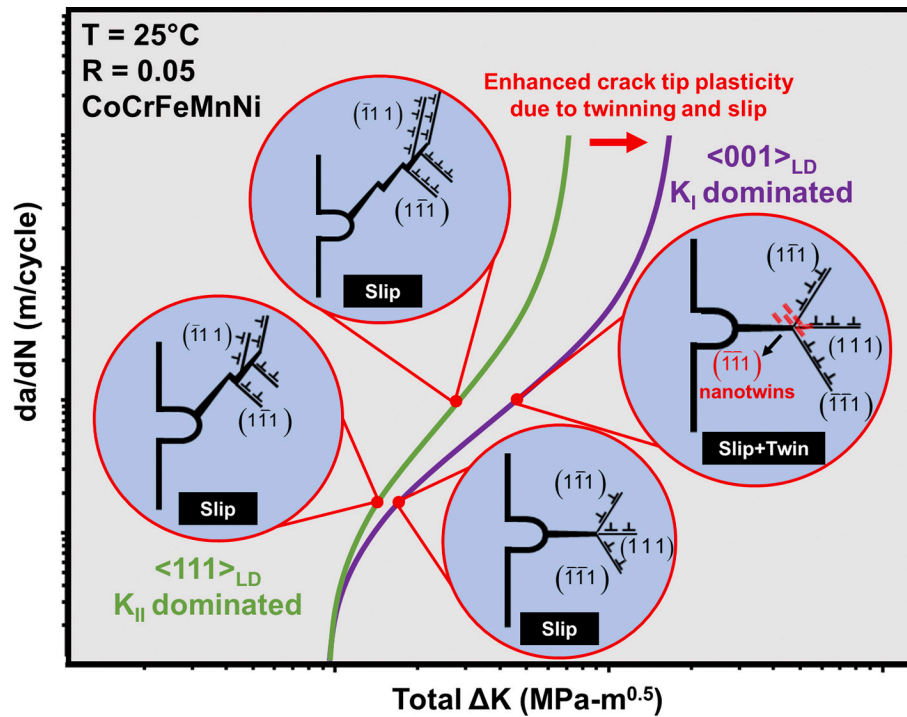
Fig. 11. Schematic describing the various deformation modes at play during the room temperature fatigue crack growth of <001> and <111> CoCrFeMnNi. Onset of additional deformation modes such as twinning delays the inception of the unstable stage III regime in fatigue crack growth and results in higher K_{max} values.

twin boundaries (CTB). Earlier in 1990 Pippan [42] introduced a model to predict fatigue threshold based on crack tip dislocation emission. It was postulated that the threshold depends on the stress intensity to emit dislocations during forward/reverse loading and the net unrecovered displacement after each fatigue cycle ahead of the crack tip (i.e. slip irreversibility). This has been recently extended to incorporated physics-based parameters such as lattice friction stress (obtained from atomistic simulations) for dislocation motion with and without the presence of barriers to dislocation motion. These fatigue models [43–45] argue that, compared to other grain boundaries, CTBs offer maximal resistance to fatigue crack growth due to under lying factors such as (i) increased lattice friction stress to move dislocations near the crack tip and (ii) enhanced slip reversibility due to the dislocation reactions occurring at the CTB. The lattice friction stress and the slip reversibility are further influenced by (i) twin thickness, (ii) twin density and (ii) slip-twin interactions. Thus, CTBs invariably increases the lattice friction stress, thereby impeding crack tip advance and enhancing the fatigue threshold. However, the lattice friction stress in the threshold regime of the single crystalline CoCrFeMnNi utilized in this study is influenced only by slip-slip interactions consistent with the FCG tests conducted in the polycrystalline samples [10,17]. Nevertheless, the benefits of twining can be realized at later stages of crack growth as discussed in the next section.

4.2. Fatigue crack growth at threshold and beyond: influence of deformation at the crack tip

Slip orientations ahead of the crack tip primarily influences the crack path and thus the crack growth rate. High resolution DIC at the notch tip (Fig. 1) indicates that two slip systems were active prior to crack growth. The ensuing crack growth in <111> loading orientation occurs at an angle along the intersection of the activated slip systems $(\bar{1}11)$ and $(1\bar{1}1)$ while periodically kinking into the $(1\bar{1}1)$ slip plane (Fig. 6a). Whereas in the <001> loading orientation, crack propagation is normal

to external stress and adheres to the intersection of two slip planes $(1\bar{1}1)$ and $(\bar{1}\bar{1}1)$. The horizontal nature of the crack propagation is further aided by the activation of a third slip plane (111) (see Fig. 4b) after crack nucleation. The crack propagation direction which determines the mode of crack growth influences the crack tip deformation as discussed below.

The crack growth rate for the considered orientations <001> and <111> varied as shown in Fig. 2a. The relatively slower crack growth rate for the <001> orientation can be attributed to various factors which include: 1) number of activate slip systems ahead of the crack tip, 2) crack tip plasticity and hardening levels, and 3) the activation of deformation twinning. Initially, prior to crack initiation, both the loading orientations exhibit the same evolution in residual strain accumulation as depicted in Fig. 1, with only two slip systems being active. As discussed in the previous paragraph, an additional slip system gets activated in the <001> orientation. Looking at Fig. 4, there is a marked difference in the strain irreversibility at the crack tip between the two orientations at a given crack length. This primarily stems from the interaction between the activated slip systems in either of the orientations. The smear in the IPF maps (Fig. 9) further validate the large lattice rotations from the original crystal orientation induced due to dislocation slip. Additionally, in <001>, the crack tip region exhibits extensive twinning. Slip-twin and twin-twin interactions, which induce additional strengthening [46,47], are evident from the local misorientation maps and TEM images shown in Fig. 5d (follow the white arrows) and 5f respectively. On the other hand, crack tip twinning in the <111> orientation is not as pronounced at an equivalent crack length. The tensile stress required to activate twinning is around 720 MPa [8] and the corresponding CRSS for twin nucleation is around 153 MPa [48]. Thus, it is fair to assume that the <001> orientation is more susceptible to crack tip twinning at relatively shorter crack lengths in comparison to <111> due to pure Mode I growth resulting in a higher resolved shear stress in the crack tip region. Also, the room temperature deformation mechanism in CoCrFeMnNi is facilitated by planar slip and intrinsic

stacking faults [8]. These stacking faults could act as a precursor to twin nucleation [49] in the <001> orientation which exhibits larger deformations at the crack tip. In conjunction, large deformations at the crack tip can alter the chemical short range order [50–52] and can further reduce the SFE [53] locally, leading to the activation of twinning. DFT calculations [54] point to the short range ordering of cobalt atoms as the driving force for twin nucleation by locally reducing the SFE in this HEA via Suzuki type interaction [55], and could possibly explain the observed crack tip twinning during room temperature fatigue crack growth.

Moreover, when considering the nominal stress vs crack tip strain plots (see Fig. 10) at various crack lengths and crack growth rates, the width of the hysteresis loops, which is an indication of plastic strain range, at the crack tip is found to be larger in the <001> orientation. By comparing the crack growth rate for <001> and <111> orientations shown in Fig. 10, it is evident that the rate is slower for <001> at a relatively equivalent crack tip strain. The slower rate can be attributed to the combined effect of high levels of strain hardening ahead of the crack tip and ductility enhancement. Interaction between multiple slip systems increases the slip irreversibility by producing kinks, jogs and Lomer-Cottrell locks [29,56] and thereby influences the crack tip hysteresis loops. Comparing the remote and local crack tip stress-strain curves shown in Fig. 10c and d, the width of the hysteresis loops in the <111> orientation is considerably lower compared to <001> indicating that the strain accumulation per cycle is smaller for <111>. Ensuing crack growth rate is thus slower for <001> as intersecting slip systems act as effective barriers to crack tip dislocations and gives rise to strain hardening of the material ahead of the crack tip. Yet, the ductility is not affected as Lomer-Cottrell locks act as dislocation nucleation sites and thereby influences the width of the hysteresis loops near the crack tip. Additionally, the massive local reorientation of the lattice at the crack tip due to twinning shear could activate slip inside the twinned volumes which were otherwise unfavorably oriented for slip prior to twinning and thus ductility is further enhanced. The presumed deformation of the nanotwins can be evidenced from the smear in the IPF map of the twinned regions (pointed out by the arrow in Fig. 9b) and the local misorientation map within the twins (pointed out by the white arrows in Fig. 5d). This conjecture was confirmed by TEM investigation of the crack tip region in <001> (Fig. 5e to h). Signatures of defects such as dislocations in single crystals appear as diffused halo around the transmitted beam in the diffraction pattern and as streaks in the diffraction spots [57]. This is clearly visible in the selected area diffraction pattern taken from the twin + matrix region (Fig. 5h). Also, the dark contrast inside the twins extending along the twinning shear direction indicates deformation of the twinned volume. On the other hand, the diffraction pattern taken from a relatively dislocation free pure matrix region, is devoid of these signatures (Fig. 5g). The TEM images also reveal that the twinned region is actually comprised of bundles of nano-twins rather than one wide twin as represented by EBSD in Fig. 5d. Physically based fatigue models, taking the energetics of dislocation-twin interactions from MD simulations as input show that nano-twins, compared to micro-twins, result in increased hardening of the matrix due to reduced mean free path between crack tip dislocations and CTB barrier, thereby resulting in increased lattice friction stress for dislocation motion [44]. Furthermore, dislocation incorporation in the CTB during slip-twin interaction preserves the ductility while synergistically enhancing hardening [44,45]. The burger's vector of the residual dislocation resulting from such interactions in CoCrFeMnNi was calculated to be $\approx$ 0.5a [16] in an earlier study which attributes the extensive strain

hardening of the matrix ahead of the crack tip resulting from the effective increase in lattice friction stress. Whereas in the <111> case, strain hardening is only influenced by strain localization in slip planes and the intersection of slip planes. The lattice reorientation is not as significant compared to <001> (see Fig. 9) signifying lower dislocation activity. Owing to the ductility enhancement and high strain hardening levels from nano-twinning, K^{max} values exceeding 230 MPa-m$^{0.5}$ was measured in the <001> orientation. This suggests that the fracture toughness, which is directly related to K^{max} in region III, of single crystalline CoCrFeMnNi could well exceed 300 MPa-m$^{0.5}$, which is akin to the values obtained in the polycrystalline counterpart [9]. Adding to the high K^{max} values and the slower crack growth rate, early onset of twinning along with enhanced slip activity in the <001> case could inevitably delay the inception of the unstable region III as schematically described in Fig. 11.

4.3. Crack tip R-ratio

Historically, experimental and theoretical fatigue crack closure studies were devoted towards fatigue crack growth in polycrystalline materials [58–61]. All the studies point to the prevalence of crack closure at R < 0.4 [62–64]. Also, these studies considered the global applied R ratio, whereas the local crack tip R ratio could be significantly different. The accumulated strain fields at the crack tip at different crack lengths would significantly affect the prevalent stress fields which is uniquely captured in this study via regression fitting of the accumulated displacement fields. Thus, in this study, the crack tip R-ratio was tracked by noting the ratio between K^{min} and K^{max} obtained via regression. The local crack tip R ratio reported in Fig. 8a shows that, at the crack tip, R > 0.6 is dominant for both the orientations even though the global R is maintained at 0.05. Consequently, crack closure is absent even when the load is removed as shown by the SEM images in Fig. 8b and c. Elber [23] theorized that the elastic material surrounding the plastic zone developed at the crack tip induces compressive tractions which overcome the globally applied tensile stress and promotes crack closure. Thus, the reasons for the crack to remain open even at minimum load in the current study suggests that these compressive tractions are not present in our case. This finding resonates with the theoretical calculations presented by Sun et al., in 1985 [65] who reported tensile residual stresses in the crack tip region as the reason for the absence of crack closure. The physical reasons for this could be that the material considered in the present study is a single crystalline high entropy alloy and the compressive tractions stemming from back stress developed due to (i) pile up of dislocations at grain boundaries and (ii) modulus mismatch of grains are absent. Additionally, the large scale plastic deformations at the crack tip may have resulted in crack tip blunting [66]. Some FEM studies show that, for a blunt crack tip, the CTOD may not completely recover during unloading and results in the absence of crack closure [39,67]. However, even when the crack is open at the minimum load, crack propagation does not occur in our case due to extensive strain hardening of the material ahead of the crack tip as discussed in the previous section. Moreover, the material being investigated here is a high entropy alloy which apparently has atoms randomly occupying the lattice sites but local short range chemical ordering of the atoms have been reported from DFT simulations [68]. Local chemical ordering near the crack tip could be significantly different from chemical ordering away from the crack tip due to considerable dislocation activity which disrupts the ordering [50–52]. As discussed in the previous section, massive deformation at the crack tip could lead to local ordering of

cobalt atoms [54] which has a smaller atomic radii compared to Cr, Fe and Mn atoms. This could in turn generate local tensile residual stresses which keeps the crack open even after the external load is removed. This process is still unclear, and more work needs to be done in this regard.

5. Conclusions

Based on the experimental findings in this study, the following conclusions can be drawn.

1. The room temperature threshold stress intensity factor for crack initiation is orientation independent and was determined as 5.5 MPa-m$^{0.5}$ for CoCrFeMnNi HEA. The corresponding local axial strain build-up in the slip systems prior to crack initiation was near 5% for <001> and <111> loading orientations.
2. By employing regression fitting of crack tip displacement fields, highest maximum crack tip stress intensity values of 230 MPa-m$^{0.5}$ and 195 MPa-m$^{0.5}$ were calculated for <001> and <111> orientations in the stage II regime respectively. Higher stress intensities and slower crack growth rate for <001> can be attributed to crack tip nano-twinning, higher slip activity and the resulting strain hardening ahead of the crack tip.
3. Crack initiation and crack propagation direction coincides with the intersection of the active slip systems and thus the crack growth was purely Mode I for <001> and mixed mode for <111>. Local crack tip R-ratio was much higher (>0.6) compared to the global R-ratio (0.05) for both the orientations and the corresponding crack tip displacement profiles and SEM images point to the absence of crack closure.

4. In <001>, the plastic accommodation enhanced by nano-twinning was further improved by the twinned volumes undergoing additional deformation as confirmed by EBSD and TEM micrographs. This activation of twinning at an earlier crack length in <001> compared to <111> could delay the onset of unstable region III and the corresponding K^{max} (fracture toughness) in region III could well exceed 300 MPa-m$^{0.5}$ for this single crystal.

CRediT authorship contribution statement

R. Sidharth: Investigation, Writing - original draft, Visualization, Formal analysis. **W. Abuzaid:** Writing - review & editing, Conceptualization, Visualization. **H. Sehitoglu:** Supervision, Conceptualization, Writing - review & editing.

Declaration of competing interest

The authors declare that they have no known competing financial interests or personal relationships that could have appeared to influence the work reported in this paper.

Acknowledgements

Appendices.

Tensile response

The uniaxial tensile response of <111> and <001> single crystals are shown below in figure A1 for completeness. The test was performed in an Instron servo hydraulic load frame at a strain rate of 10^{-4} s^{-1}. Yield strengths for the <111> and <001> orientations were 170 MPa and 150 MPa respectively.
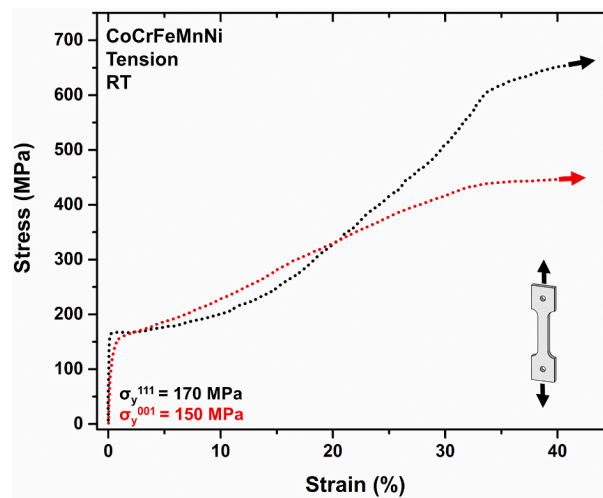
Fig. A1. Tensile response of <111> and <001> single crystals at RT.

Regression analysis

The full field displacement measurements from DIC were used for obtaining the stress intensity change per fatigue cycle. A non-linear least squares regression procedure was carried out to fit the experimental vertical and horizontal displacement fields to the analytical description of the displacement fields given by Sih et al. [27]. These are given as,

$$u = K_I \sqrt{\frac{2r}{\pi}} \text{Re} \left[\frac{1}{\mu_1 - \mu_2} \left\{ \mu_1 p_2 \sqrt{\cos\theta + \mu_2 \sin\theta} - \mu_2 p_1 \sqrt{\cos\theta + \mu_1 \sin\theta} \right\} \right] +$$

$$K_{II} \sqrt{\frac{2r}{\pi}} \text{Re} \left[\frac{1}{\mu_1 - \mu_2} \left\{ p_2 \sqrt{\cos\theta + \mu_2 \sin\theta} - p_1 \sqrt{\cos\theta + \mu_1 \sin\theta} \right\} \right] + a_{11} Tr \cos\theta + Ar \sin\theta + B_u \tag{A1}$$

$$v = K_I \sqrt{\frac{2r}{\pi}} \text{Re} \left[\frac{1}{\mu_1 - \mu_2} \left\{ \mu_1 q_2 \sqrt{\cos\theta + \mu_2 \sin\theta} - \mu_2 q_1 \sqrt{\cos\theta + \mu_1 \sin\theta} \right\} \right] +$$

$$K_{II} \sqrt{\frac{2r}{\pi}} \text{Re} \left[\frac{1}{\mu_1 - \mu_2} \left\{ q_2 \sqrt{\cos\theta + \mu_2 \sin\theta} - q_1 \sqrt{\cos\theta + \mu_1 \sin\theta} \right\} \right] + a_{12} Tr \sin\theta + Ar \cos\theta + B_v \tag{A2}$$

where 'u' denotes horizontal displacement, 'v' denotes vertical displacement with respect to the crack coordinate frame as shown in the schematic figure A2. 'Re' denotes the real part of a complex number. Further, p_j and q_j are given as,

$$p_j = a_{11} \mu_j^2 + a_{12} - a_{16} \mu_j \tag{A3}$$

$$q_j = a_{12} \mu_j + \frac{a_{22}}{\mu_j} - a_{26} \tag{A4}$$
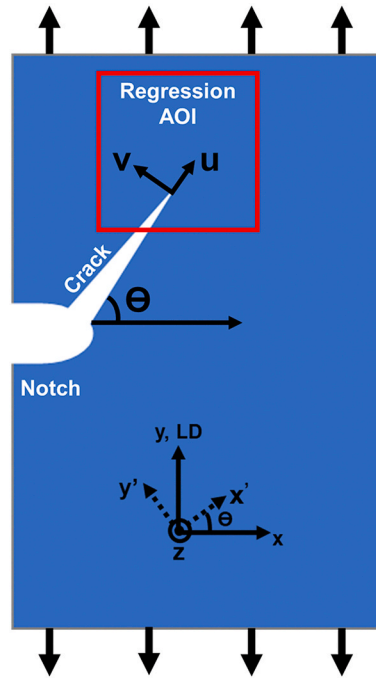
Fig. A2. Schematic depicting the regression AOI, vertical (v) and horizontal displacement (u) in the crack coordinate system. Θ is the crack inclination angle.

The extracted quantities from the regression fit are K_I and K_{II} which represent the Mode I and Mode II stress intensity factors respectively, T is the T-stress, A is the rigid body rotation, B_u and B_v are the rigid body translations in the u, v direction respectively, r and Θ are the polar coordinates with the origin at the crack tip. μ_1 and μ_2 are the complex roots of the characteristic equation,

$$a_{11} \mu^4 - 2a_{16} \mu^3 + (2a_{12} + a_{66}) \mu^2 - 2a_{26} \mu + a_{22} = 0 \tag{A5}$$

where a_{ij} are the compliance constants of CoCrFeMnNi in the crack coordinate frame obtained by rotating the compliance constants $S_{11} = 0.00754$ GPa^{-1}, $S_{12} = -0.00285$ GPa^{-1} and $S_{44} = 0.00522$ GPa^{-1} [35] given in the global coordinate frame. Once K_I and K_{II} were both obtained, the total stress intensity factor for mixed mode growth was calculated as described in the results section 3.2.

References

[1] D.B. Miracle, O.N. Senkov, A critical review of high entropy alloys and related concepts, Acta Mater. 122 (2017) 448–511.

[2] M.-H. Tsai, J.-W. Yeh, High-entropy alloys: a critical review, Mater. Res. Lett. 2 (3) (2014) 107–123.

[3] E.P. George, D. Raabe, R.O. Ritchie, High-entropy alloys, Nat. Rev. Mater. 4 (8) (2019) 515–534.

[4] W. Abuzaid, H. Sehitoglu, Plastic strain partitioning in dual phase Al13CoCrFeNi high entropy alloy, Mater. Sci. Eng., A 720 (2018) 238–247.

[5] J.W. Yeh, S.K. Chen, S.J. Lin, J.Y. Gan, T.S. Chin, T.T. Shun, C.H. Tsau, S.Y. Chang, Nanostructured high-entropy alloys with multiple principal elements: novel alloy design concepts and outcomes, Adv. Eng. Mater. 6 (5) (2004) 299–303.

[6] O. Senkov, J. Scott, S. Senkova, D. Miracle, C. Woodward, Microstructure and room temperature properties of a high-entropy TaNbHfZrTi alloy, J. Alloys Compd. 509 (20) (2011) 6043–6048.

[7] B. Cantor, I. Chang, P. Knight, A. Vincent, Microstructural development in equiatomic multicomponent alloys, Mater. Sci. Eng., A 375 (2004) 213–218.

[8] F. Otto, A. Dlouhý, C. Somsen, H. Bei, G. Eggeler, E.P. George, The influences of temperature and microstructure on the tensile properties of a CoCrFeMnNi high-entropy alloy, Acta Mater. 61 (15) (2013) 5743–5755.

[9] B. Gludovatz, A. Hohenwarter, D. Catoor, E.H. Chang, E.P. George, R.O. Ritchie, A fracture-resistant high-entropy alloy for cryogenic applications, Science 345 (6201) (2014) 1153–1158.

[10] K.V. Thurston, B. Gludovatz, Q. Yu, G. Laplanche, E.P. George, R.O. Ritchie, Temperature and load-ratio dependent fatigue-crack growth in the CrMnFeCoNi high-entropy alloy, J. Alloys Compd. 794 (2019) 525–533.

[11] M. Yao, K.G. Pradeep, C.C. Tasan, D. Raabe, A novel, single phase, non-equiatomic FeMnNiCoCr high-entropy alloy with exceptional phase stability and tensile ductility, Scripta Mater. 72 (2014) 5–8.

[12] N. Stepanov, M. Tikhonovsky, N. Yurchenko, D. Zyabkin, M. Klimova, S. Zherebtsov, A. Efimov, G. Salishchev, Effect of cryo-deformation on structure and properties of CoCrFeNiMn high-entropy alloy, Intermetallics 59 (2015) 8–17.

[13] N. Kashaev, V. Ventzke, N. Petrov, M. Horstmann, S. Zherebtsov, D. Shaysultanov, V. Sanin, N. Stepanov, Fatigue behaviour of a laser beam welded CoCrFeNiMn-type high entropy alloy, Mater. Sci. Eng., A 766 (2019), 138358.

[14] A. Hamada, L. Karjalainen, J. Puustinen, Fatigue behavior of high-Mn TWIP steels, Mater. Sci. Eng., A 517 (1–2) (2009) 68–77.

[15] T. Niendorf, F. Rubitschek, H. Maier, J. Niendorf, H. Richard, A. Frehn, Fatigue crack growth—microstructure relationships in a high-manganese austenitic TWIP steel, Mater. Sci. Eng., A 527 (9) (2010) 2412–2417.

[16] M. Bönisch, Y. Wu, H. Sehitoglu, Hardening by slip-twin and twin-twin interactions in FeMnNiCoCr, Acta Mater. 153 (2018) 391–403.

[17] K.V. Thurston, B. Gludovatz, A. Hohenwarter, G. Laplanche, E.P. George, R. O. Ritchie, Effect of temperature on the fatigue-crack growth behavior of the high-entropy alloy CrMnFeCoNi, Intermetallics 88 (2017) 65–72.

[18] P. Neuman, New experiments concerning the slip processes at propagating fatigue cracks-I, Acta Metall. 22 (1974) 1155–1165.

[19] C. Laird, G. Smith, Crack propagation in high stress fatigue, Phil. Mag. 7 (77) (1962) 847–857.

[20] E. Orowan, Fracture and strength of solids, Rep. Prog. Phys. 12 (1) (1949), 185.

[21] P. Forsyth, Some results of the examination of aluminum alloy specimen fracture surfaces, Metal 63 (1961) 117–124.

[22] R.O. Ritchie, Mechanisms of fatigue-crack propagation in ductile and brittle solids, Int. J. Fract. 100 (1) (1999) 55–83.

[23] E. Wolf, Fatigue crack closure under cyclic tension, Eng. Fract. Mech. 2 (1) (1970) 37–45.

[24] W. Elber, The Significance of Fatigue Crack Closure, Damage Tolerance in Aircraft Structures, ASTM International, 1971.

[25] J.E. Allison, R.C. Ku, M.A. Pompetzki, A Comparison of Measurement Methods and Numerical Procedures for the Experimental Characterization of Fatigue Crack Closure, Mechanics of Fatigue Crack Closure, ASTM International, 1988.

[26] M.A. Sutton, W. Zhao, S.R. McNeill, J.D. Helm, R.S. Piascik, W.T. Riddell, Local Crack Closure Measurements: Development of a Measurement System Using Computer Vision and a Far-Field Microscope, Advances in Fatigue Crack Closure Measurement and Analysis, second volume, ASTM International, 1999.

[27] G.C. Sih, P. Paris, G.R. Irwin, On cracks in rectilinearly anisotropic bodies, Int. J. Fract. Mech. 1 (3) (1965) 189–203.

[28] S. Yoneyama, Y. Morimoto, M. Takashi, Automatic evaluation of mixed-mode stress intensity factors utilizing digital image correlation, Strain 42 (1) (2006) 21–29.

[29] G.J. Pataky, M.D. Sangid, H. Sehitoglu, R.F. Hamilton, H.J. Maier, P. Sofronis, Full field measurements of anisotropic stress intensity factor ranges in fatigue, Eng. Fract. Mech. 94 (2012) 13–28.

[30] E. Sgambitterra, C. Maletta, F. Furgiuele, H. Sehitoglu, Fatigue crack propagation in [0 1 2] NiTi single crystal alloy, Int. J. Fatig. 112 (2018) 9–20.

[31] Y. Wu, A. Ojha, L. Patriarca, H. Sehitoglu, Fatigue crack growth fundamentals in shape memory alloys, Shape Memory Superelasticity 1 (1) (2015) 18–40.

[32] G. Laplanche, S. Berglund, C. Reinhart, A. Kostka, F. Fox, E. George, Phase stability and kinetics of σ-phase precipitation in CrMnFeCoNi high-entropy alloys, Acta Mater. 161 (2018) 338–351.

[33] J.D. Carroll, W. Abuzaid, J. Lambros, H. Sehitoglu, High resolution digital image correlation measurements of strain accumulation in fatigue crack growth, Int. J. Fatig. 57 (2013) 140–150.

[34] J. Carroll, C. Efstathiou, J. Lambros, H. Sehitoglu, B. Hauber, S. Spottswood, R. Chona, Investigation of fatigue crack closure using multiscale image correlation experiments, Eng. Fract. Mech. 76 (15) (2009) 2384–2398.

[35] H. Zhang, X. Sun, S. Lu, Z. Dong, X. Ding, Y. Wang, L. Vitos, Elastic properties of AlxCrMnFeCoNi (0≤ x≤ 5) high-entropy alloys from ab initio theory, Acta Mater. 155 (2018) 12–22.

[36] K. Tanaka, Fatigue crack propagation from a crack inclined to the cyclic tensile axis, Eng. Fract. Mech. 6 (3) (1974) 493–507.

[37] S. Rabbolini, G. Pataky, H. Sehitoglu, S. Beretta, Fatigue crack growth in Haynes 230 single crystals: an analysis with digital image correlation, Fatig. Fract. Eng. Mater. Struct. 38 (5) (2015) 583–596.

[38] M. Beghini, L. Bertini, Fatigue crack propagation through residual stress fields with closure phenomena, Eng. Fract. Mech. 36 (3) (1990) 379–387.

[39] V. Tvergaard, On fatigue crack growth in ductile materials by crack–tip blunting, J. Mech. Phys. Solid. 52 (9) (2004) 2149–2166.

[40] M.D. Sangid, H.J. Maier, H. Sehitoglu, The role of grain boundaries on fatigue crack initiation–an energy approach, Int. J. Plast. 27 (5) (2011) 801–821.

[41] K. Tanaka, K. Mura, A Dislocation Model for Fatigue Crack Initiation, ASME. J. Appl. Mech. 48 (1) (1981) 97–103.

[42] R. Pippan, Dislocation emission and fatigue crack growth threshold, Acta Metall. Mater. 39 (3) (1991) 255–262.

[43] S. Alkan, H. Sehitoglu, Nonuniqueness of the fatigue threshold, Int. J. Fatig. 104 (2017) 309–321.

[44] S. Alkan, P. Chowdhury, H. Sehitoglu, R.G. Rateick, H.J. Maier, Role of nanotwins on fatigue crack growth resistance–experiments and theory, Int. J. Fatig. 84 (2016) 28–39.

[45] P.B. Chowdhury, H. Sehitoglu, R.G. Rateick, H.J. Maier, Modeling fatigue crack growth resistance of nanocrystalline alloys, Acta Mater. 61 (7) (2013) 2531–2547.

[46] I. Karaman, H. Sehitoglu, A. Beaudoin, Y.I. Chumlyakov, H. Maier, C. Tome, Modeling the deformation behavior of Hadfield steel single and polycrystals due to twinning and slip, Acta Mater. 48 (9) (2000) 2031–2047.

[47] K. Raghavan, A. Sastri, M. Marcinkowski, Nature of the work-hardening behavior in hadfields manganese steel, Trans. Met. Soc. AIME 245 (7) (1969) 1569–1575.

[48] W. Abuzaid, H. Sehitoglu, Critical resolved shear stress for slip and twin nucleation in single crystalline FeNiCoCrMn high entropy alloy, Mater. Char. 129 (2017) 288–299.

[49] I. Karaman, H. Sehitoglu, Y.I. Chumlyakov, H. Maier, I. Kireeva, Extrinsic stacking faults and twinning in Hadfield manganese steel single crystals, Scripta Mater. 44 (2) (2001) 337–343.

[50] V. Gerold, H. Karnthaler, On the origin of planar slip in fcc alloys, Acta Metall. 37 (8) (1989) 2177–2183.

[51] J. Olfe, H. Neuhäuser, Dislocation groups, multipoles, and friction stresses in α-CuZn alloys, Phys. Status Solidi 109 (1) (1988) 149–160.

[52] J. Plessing, C. Achmus, H. Neuhäuser, B. Schönfeld, G. Kostorz, Short-range order and the mode of slip in concentrated Cu-based alloys, Z. Metallkd. 88 (8) (1997) 630–635.

[53] J. Ding, Q. Yu, M. Asta, R.O. Ritchie, Tunable stacking fault energies by tailoring local chemical order in CrCoNi medium-entropy alloys, Proc. Natl. Acad. Sci. Unit. States Am. 115 (36) (2018) 8919–8924.

[54] S. Alkan, A. Ojha, H. Sehitoglu, Determination of latent hardening response for FeNiCoCrMn for twin-twin interactions, Acta Mater. 147 (2018) 149–164.

[55] H. Suzuki, Segregation of solute atoms to stacking faults, J. Phys. Soc. Jpn. 17 (2) (1962) 322–325.

[56] J. Hirth, On dislocation interactions in the fcc lattice, J. Appl. Phys. 32 (4) (1961) 700–706.

[57] M.A. Asadabad, M.J. Eskandari, Electron Diffraction, Modern Electron Microscopy in Physical and Life Sciences, 2016, pp. 3–24.

[58] R. McClung, H. Sehitoglu, On the finite element analysis of fatigue crack closure—1. Basic modeling issues, Eng. Fract. Mech. 33 (2) (1989) 237–252.

[59] R. McClung, H. Sehitoglu, On the finite element analysis of fatigue crack closure—2. Numerical results, Eng. Fract. Mech. 33 (2) (1989) 253–272.

[60] K. Solanki, S. Daniewicz, J. Newman Jr., Finite element analysis of plasticity-induced fatigue crack closure: an overview, Eng. Fract. Mech. 71 (2) (2004) 149–171.

[61] H. Staal, J. Elen, Crack closure and influence of cycle ratio R on fatigue crack growth in type 304 stainless steel at room temperature, Eng. Fract. Mech. 11 (2) (1979) 275–283.

[62] H. Sehitoglu, Crack opening and closure in fatigue, Eng. Fract. Mech. 21 (2) (1985) 329–339.

[63] S. Suresh, Fatigue of Materials, Cambridge university press, 1998.

[64] R.C. McClung, J. Newman, Advances in Fatigue Crack Closure Measurement and Analysis, second volume, ASTM, 1999.

[65] W. Sun, H. Sehitoglu, Residual stress fields during fatigue crack growth, Fatig. Fract. Eng. Mater. Struct. 15 (2) (1992) 115–128.

[66] T. Shoji, Crack-tip blunting and crack-opening displacement under large-scale yielding, Met. Sci. 10 (5) (1976) 165–169.

[67] I. Gu, R. Ritchie, On the crack-tip blunting model for fatigue crack propagation in ductile materials, Fatigue Fract. Mech. 29th (1999). ASTM International.

[68] P. Singh, A.V. Smirnov, D.D. Johnson, Atomic short-range order and incipient long-range order in high-entropy alloys, Phys. Rev. B 91 (22) (2015), 224204.